

Impurity flat band states in the diamond chain

A. M. Marques,^{1,*} D. Viedma,² V. Ahufinger,² and R. G. Dias¹

¹*Department of physics & i3N, University of Aveiro, 3810-193 Aveiro, Portugal*

²*Departament de Física, Universitat Autònoma de Barcelona, E-08193 Bellaterra, Spain*

Flat band (FB) systems, *i.e.*, models hosting dispersionless bands in their energy spectrum, have attracted great interest recently. The eigenstates of these FBs can be written as compact localized states (CLSs), meaning states having finite support only over a small, non-extensive portion of the lattice. When adjacent CLSs of a FB have spatial overlap, the subspace they span is, in general, non-orthogonal. Here, we consider precisely this scenario, in the form of a diamond chain with a finite magnetic flux per plaquette, which has a gapped midspectrum FB. After developing the general framework for projecting arbitrary operators onto a non-orthogonal subspace, we address the case of an open chain with small local impurities in the midchain plaquette. The framework is then applied to derive analytical expressions for the states of the FB affected by the impurities. The results are illustrated for three representative cases: two equal impurities, two symmetric impurities, and a single impurity. We also address the effects of diagonal disorder on the impurity states. Focusing on the equal impurities case, we show how these states effectively feel an averaged disorder determined by their spatial extension, which can be controlled by the flux. Due to this averaging effect, these states exhibit enhanced robustness to disorder. For the single-impurity case, we further reveal its exotic non-trivial topological phase, without precedent in the literature on Hermitian models, characterized by a half-integer winding number. By mapping the system onto an equivalent two-dimensional (2D) tight-binding lattice decorated with a central impurity line, the half-integer bulk invariants are shown to have a correspondence with the appearance of a single in-gap edge state when open boundary conditions (OBC) are imposed. Numerical simulations are performed to benchmark all analytical predictions, showing a near-perfect agreement for flux values away from the gap closing point. Our results lay the foundation for further inquiries on the physics of non-orthogonal bases, and are expected to be of particular relevance to the study of FB related phenomena.

I. INTRODUCTION

About a decade ago, a renewed interest in FB systems [1] gave way to a new cycle of studies devoted to the topic (a more detailed chronology can be found in [2]), and it has no signs of slowing down. In this new wave of studies, the focus has gradually shifted towards the CLSs that span every FB. For one-dimensional (1D) models, it has been shown that these CLSs form an orthogonal set when the FB projector is strictly local, and a non-orthogonal one otherwise [3, 4]. Based on the form of the CLSs, FB generators were constructed for 1D [5, 6] and higher-dimensional [7–11] models.

An interesting class of FB systems is the (self-explanatory) class of all-bands-flat (ABF) models [12, 13], where transport is completely suppressed, since any local excitation in an ABF model can be written as a linear combination of CLSs belonging to the different FBs, leading to the phenomenon of particle confinement known as Aharonov-Bohm (AB) caging [14]. The diamond chain with a π -flux per plaquette [15–20], along with its 2^n -root versions [21, 22], is a prime example of an ABF model exhibiting AB caging that has been thoroughly investigated. In this and other related ABF models, the effects of weak perturbations have been studied by projecting the perturbation operator onto one of the

FBs. For example, this method was employed to study weak disorder in the ABF Creutz ladder [23, 24], and weak interactions in both this model [25] and the diamond chain [26], shown to be able to induce dynamical effects [27] in two-body states where it would otherwise be absent, due to the infinite effective mass of the states of a FB. Conversely, strong interactions can drive the appearance of effective ABF many-body subspaces, in models with a dispersive single-particle energy spectrum [28].

Here, we address the case of a diamond chain with a finite flux per plaquette, and introduce a perturbation in the form of weak local potentials in the midchain plaquette, as schematically illustrated in Fig. 1(a). By projecting this impurity perturbation onto the gapped zero-energy FB, only two partially overlapping CLSs have finite weight at the impurity sites. However, due to the non-orthogonal nature of adjacent CLSs, we show that the analytical treatment of the system requires one to re-express the problem in terms of its dual basis states. This greatly simplifies the problem, by reducing it to the solutions of a decoupled dimer in a non-orthogonal dual subspace. We then derive the analytical solutions for the impurity states that are lifted from the FB as a function of the magnetic flux, focusing on the cases of two equal impurities, two symmetric impurities, and a single-impurity, where near-perfect agreement with numerical results is observed. Finally, for the single-impurity case, we further demonstrate how it corresponds to a non-trivial topological phase characterized by half-integer topological invari-

* anselmomagalhaes@ua.pt

ants. Upon mapping this system onto an equivalent 2D lattice decorated with a central line of defects, we provide indirect evidence of a refined bulk-boundary correspondence by relating the half-integer bulk invariants with the presence of a single in-gap edge state in the spectrum of the mapped lattice.

The rest of the paper is organized as follows. In Sec. II, we provide a brief overview on the theory of non-orthogonal bases, with an emphasis on how to project an operator onto such bases, and how to orthonormalize them by means of the Löwdin transformation [29]. In Sec. III, we introduce the model considered in this study, namely the diamond chain threaded by a finite flux per plaquette, in its clean version, deriving its solutions and the form of the overlap matrix for the CLSs spanning the zero-energy FB. In Sec. IV, we perturb the model by including weak local impurities in the top and bottom sites of the midchain plaquette, deriving the general analytical expression for the impurity states that come off the FB, using the techniques described in Sec. II. After that, we analyze in greater detail the particular cases of equal impurities, symmetric impurities, and single-impurity. For the latter, we also study its peculiar topological features, whose physical manifestation requires the introduction of an equivalent 2D lattice for its observation. Lastly, we present our conclusions in Sec. V.

II. BASICS OF NON-ORTHOGONAL BASES

In this section, we will review some basic results of non-orthogonal bases, particularly in what concerns the definition of projection operators and the procedure for diagonalizing a Hamiltonian written in such a basis. We will heavily rely in the theory outlined in [30], as well in the summarized results provided in the appendix of [31]. Let us start by considering a non-orthogonal basis $\{|i\rangle\}$, not necessarily normalized. The elements of the overlap matrix \mathbf{S} of this basis are written as $S_{ij} = \langle i|j\rangle$, with \mathbf{S} further assumed to be a real symmetric matrix $S_{ij} = S_{ji}$. Evidently, \mathbf{S} reduces to the identity \mathbf{I} for an orthonormal basis. One can define the dual basis $\{|i^*\rangle\}$, whose states are defined by the property $\langle i|j^*\rangle = \delta_{ij}$, with δ_{ij} the Kronecker delta. The transformation of states between the direct and dual bases is given by

$$|i\rangle = \sum_j S_{ij} |j^*\rangle, \quad |i^*\rangle = \sum_j S_{ij}^{-1} |j\rangle, \quad (1)$$

where the usual slight abuse of language of writing $(\mathbf{S}^{-1})_{ij}$ as S_{ij}^{-1} is used here and throughout the text for simplicity. The identity operator can therefore be expressed in several different forms, as

$$\hat{I} = \sum_i |i\rangle \langle i^*| = \sum_{ij} |i\rangle S_{ij}^{-1} \langle j|, \quad (2)$$

which is widely used, e.g., in systems of coupled coherent states [32, 33] that form an overcomplete non-orthogonal

basis, or alternatively as

$$\hat{I} = \sum_i |i^*\rangle \langle i| = \sum_{ij} |i^*\rangle S_{ij} \langle j^*|. \quad (3)$$

From $\hat{I}^2 = \hat{I}$, one can derive the following useful identity,

$$\sum_k S_{ik}^{-1} S_{kj} = \delta_{ij}. \quad (4)$$

A. Projection of operators onto a non-orthogonal subspace

It is convenient, for later use, to consider the case of a basis of size $N + M$ composed of two orthogonal subspaces, $\{|i\rangle\} = \{|\text{Loc}, n\rangle\} \cup \{|\text{Ext}, m\rangle\}$, with $n = 1, 2, \dots, N$ and $m = 1, 2, \dots, M$, and where, anticipating the notation that will be used later on, $\{|\text{Loc}, n\rangle\}$ stands for the non-orthogonal subspace of localized states and $\{|\text{Ext}, m\rangle\}$ for the orthonormal subspace of extended states. The total overlap matrix reads as $\mathbf{S}_{\text{tot}} = \mathbf{S} \oplus \mathbf{I}_M$, where \mathbf{I}_M is the identity matrix of size M . The projection operator onto the non-orthogonal subspace is written as

$$\begin{aligned} \hat{P}_{\text{Loc}} &= \sum_{j=1}^N |\text{Loc}, j\rangle \langle \text{Loc}, j^*| \\ &= \sum_{j=1}^N |\text{Loc}, j\rangle \sum_{i=1}^{N+M} S_{ij}^{-1} \langle i| \\ &= \sum_{i,j=1}^N |\text{Loc}, j\rangle S_{ij}^{-1} \langle \text{Loc}, i|, \end{aligned} \quad (5)$$

where $|\text{Loc}, j^*\rangle$ belongs to the dual localized subspace and the orthogonality between subspaces was used in the last line. Correspondingly,

$$\begin{aligned} \hat{P}_{\text{Loc}}^\dagger &= \sum_{j=1}^N |\text{Loc}, j^*\rangle \langle \text{Loc}, j| \\ &= \sum_{i,j=1}^N |\text{Loc}, i\rangle S_{ij}^{-1} \langle \text{Loc}, j| = \hat{P}_{\text{Loc}}. \end{aligned} \quad (6)$$

Given an arbitrary operator \hat{A} , its projection onto the non-orthogonal subspace can be developed as

$$\begin{aligned} \hat{A}_{\text{Loc}} &= \hat{P}_{\text{Loc}}^\dagger \hat{A} \hat{P}_{\text{Loc}} \\ &= \sum_{i,j=1}^N |\text{Loc}, i^*\rangle A_{ij} \langle \text{Loc}, j^*|, \end{aligned} \quad (7)$$

where $A_{ij} = \langle \text{Loc}, i| \hat{A} |\text{Loc}, j\rangle$.

B. Symmetric orthonormalization

Given a non-orthogonal basis, one can always find an orthonormalized basis through the Gram-Schmidt

method [34], which relies on a recursive state-by-state orthogonalization procedure. However, this method can be very computationally demanding and prone to numerical instabilities. A more efficient method consists of using the Löwdin transformation [29, 35] to perform a symmetrical orthogonalization of a non-orthogonal basis. With this transformation, and from a non-orthogonal basis spanning $\{|i\rangle\}$, with $i = 1, 2, \dots, N$, one can find the orthogonal basis states with the help of the overlap matrix as

$$|\tilde{i}\rangle = \sum_j S_{ij}^{-\frac{1}{2}} |j\rangle, \quad (8)$$

where, again, we use the simplified notation $S_{ij}^{-\frac{1}{2}} \equiv (S^{-\frac{1}{2}})_{ij}$. The secular equation, in this basis, is computed through the effective Hamiltonian $\tilde{\mathbf{H}}$,

$$\tilde{\mathbf{H}}\tilde{\psi}_j = E_j\tilde{\psi}_j, \quad j = 1, 2, \dots, N, \quad (9)$$

$$\tilde{\mathbf{H}} = \mathbf{S}^{-\frac{1}{2}}\mathbf{H}\mathbf{S}^{-\frac{1}{2}}, \quad (10)$$

where \mathbf{H} is the Hamiltonian matrix written in the starting non-orthogonal $\{|i\rangle\}$ basis, also called the core Hamiltonian [36], and $\tilde{\psi}_j$ is the j^{th} eigenvector with components spanning the orthogonal $\{|\tilde{i}\rangle\}$ basis.

III. DIAMOND CHAIN WITH FLUX

The specific system we will consider from now on will be that of Fig. 1(a), consisting of a diamond chain with a $\phi = 2\pi\frac{\Phi}{\Phi_0}$ reduced magnetic flux per plaquette, with Φ the magnetic flux and Φ_0 the magnetic flux quantum. Setting the lattice constant to unit, the bulk Hamiltonian of the clean system is given, in the $\{|A(k)\rangle, |B(k)\rangle, |C(k)\rangle\}$ basis, with k the quasimomentum, by

$$H(k) = -t \begin{pmatrix} 0 & h \\ h^\dagger & 0 \end{pmatrix}, \quad (11)$$

$$h^\dagger = \begin{pmatrix} e^{i\frac{\phi}{4}} + e^{i(k-\frac{\phi}{4})} \\ e^{-i\frac{\phi}{4}} + e^{i(k+\frac{\phi}{4})} \end{pmatrix} \quad (12)$$

where t is the magnitude of the hopping term. Diagonalization of this Hamiltonian yields three energy bands,

$$E_0 = 0, \quad (13)$$

$$E_{\pm}(k) = \pm 2t\sqrt{1 + \cos k \cos \frac{\phi}{2}}, \quad (14)$$

where $E_{\pm}(k)$ are dispersive for all ϕ except for $\phi = \pi$, where they become flat [see Fig. 1(b)]. An energy gap between the zero-energy FB E_0 and $E_{\pm}(k)$ opens at $k = \pi$ for $\phi \neq 0$, with a value of $E_{\text{gap}} = 2t\sqrt{1 + \cos \frac{\phi}{2}}$.

The eigenstates corresponding to E_0 can be written as CLSs, which for finite flux span over two plaquettes [18], as shown in Fig. 1(a). Consecutive normalized CLSs of the zero-energy FB are written, in the

$\{|B_j\rangle, |C_j\rangle, |B_{j+1}\rangle, |C_{j+1}\rangle, |B_{j+2}\rangle, |C_{j+2}\rangle\}$ basis, where $|\zeta_l\rangle$ stands for the state at site $\zeta = B, C$ of unit cell l (note that A sites are absent from this basis, as the CLSs have no weight on them), as

$$|\text{Loc}, j\rangle = \frac{1}{2}(1, -e^{-i\frac{\phi}{2}}, e^{-i\frac{\phi}{2}}, -1, 0, 0)^T, \quad (15)$$

$$|\text{Loc}, j+1\rangle = \frac{1}{2}(0, 0, 1, -e^{-i\frac{\phi}{2}}, e^{-i\frac{\phi}{2}}, -1)^T, \quad (16)$$

which overlap in the two middle sites [see Fig. 1(a)]. By taking advantage of this overlap, it was already shown that projecting spatially modulated onsite interactions on the CLSs can induce topological behavior in a two-body system [26]. Here, we will focus on the single-particle case. The elements of the overlap matrix within

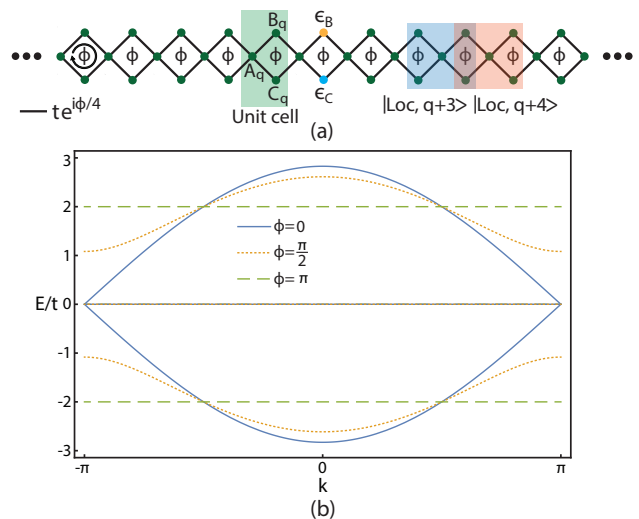


Figure 1. (a) Diamond chain with ϕ flux per plaquette, distributed uniformly by the four hopping terms of each plaquette, with positive phase accumulated in the clockwise direction. Green shaded region represents the q^{th} unit cell with sites A_q , B_q and C_q , while blue and orange shaded regions represent the spatial width of adjacent CLSs $|\text{Loc}, q+3\rangle$ and $|\text{Loc}, q+4\rangle$, respectively, which overlap in the middle B and C sites. Onsite impurity potentials ϵ_B and ϵ_C are placed at the orange B_{q+1} and light blue C_{q+1} sites, respectively. (b) Bulk energy spectrum, in units of t , of the diamond chain for three representative values of the ϕ flux per plaquette. The zero-energy flat band is common to all ϕ values.

the non-orthogonal subspace of CLSs of the zero-energy FB, $S_{ij} = \langle \text{Loc}, i | \text{Loc}, j \rangle$, are given, using (15)-(16), by

$$\begin{cases} S_{jj} = 1, \\ S_{jj+1} = S_{j+1j} = \frac{1}{2} \cos \frac{\phi}{2}, \\ S_{ij} = 0, |i-j| > 1, \end{cases} \quad (17)$$

states in the orthogonalized set $\{|\text{Loc}, l\rangle\}$ will have a *finite weight* at the $q+1$ plaquette where the impurities are located, such that, from (24), we will have $V_{nm} \neq 0$ at least for some $n, m \neq q, q+1$, and the effective model is not restricted to two states in the original basis. On the other hand, the impurity operator of the dual basis, given in (26), is not spatially defined, but instead directly couples the q and $q+1$ dual CLSs. As such, regardless of the particular spatial profile of the dual states in the orthogonalized $\{|\text{Loc}, l^*\rangle\}$ set, all effective impurity elements involving these states, computed from (26), will vanish, given that they are assumed orthogonal to the $\{|\text{Loc}, q^*\rangle, |\text{Loc}, q+1^*\rangle\}$ states appearing in \hat{V}_{FB} . Therefore, working in the dual basis greatly simplifies the problem, now reduced to the diagonalization of a dimer model defined in a two-state dual basis.

Since the two-state dual basis $\{|\text{Loc}, q^*\rangle, |\text{Loc}, q+1^*\rangle\}$ is itself non-orthogonal, we first need to orthogonalize it through the Löwdin transformation [29, 35], as outlined in Sec. II B. The first step requires us to find the form of $\mathbf{S}_*^{-\frac{1}{2}}$, where \mathbf{S}_* is the overlap matrix written in this basis. Using (1), it is straightforward to show that the elements of \mathbf{S}_* can be expressed as

$$\begin{aligned} S_{*,nm} &= \langle \text{Loc}, n^* | \text{Loc}, m^* \rangle \\ &= \sum_{i,j} S_{ni}^{-1} \langle \text{Loc}, i | \text{Loc}, j \rangle S_{jm}^{-1} \\ &= \sum_j \left(\sum_i S_{ni}^{-1} S_{ij} \right) S_{jm}^{-1} \\ &= \sum_j \delta_{nj} S_{jm}^{-1} \\ &= S_{nm}^{-1}, \end{aligned} \quad (27)$$

where (4) was used in the fourth line. Using $q = \frac{N}{2}$ and assuming the thermodynamic limit ($N \rightarrow \infty$), such that $\sinh[x(N)] \rightarrow \frac{e^x(N)}{2}$ in (22)-(23), we obtain the following expressions for some elements of the inverse overlap

$$V_{*,qq} = V_{*,q+1q+1} = v[(S_{qq}^{-1})^2 + (S_{qq+1}^{-1})^2] + (w + \bar{w})S_{qq}^{-1}S_{qq+1}^{-1}, \quad (33)$$

$$V_{*,q+1q} = V_{*,q+1q}^* = \bar{w}(S_{qq}^{-1})^2 + w(S_{qq+1}^{-1})^2 + 2vS_{qq}^{-1}S_{qq+1}^{-1}, \quad (34)$$

where \bar{w} is the complex conjugate of w . According to

$$\begin{aligned} \tilde{\mathbf{V}}_{FB} &= \mathbf{S}_*^{-\frac{1}{2}} \mathbf{V}_{FB} \mathbf{S}_*^{-\frac{1}{2}} \\ &= \begin{pmatrix} \frac{\epsilon_B + \epsilon_C}{4} & \frac{\epsilon_B + \epsilon_C}{4} e^{-\theta} + i \frac{\epsilon_B - \epsilon_C}{4} \sqrt{1 - e^{-2\theta}} \\ \frac{\epsilon_B + \epsilon_C}{4} e^{-\theta} - i \frac{\epsilon_B - \epsilon_C}{4} \sqrt{1 - e^{-2\theta}} & \frac{\epsilon_B + \epsilon_C}{4} \end{pmatrix}. \end{aligned} \quad (35)$$

Diagonalization of this matrix yields, through (21), the

matrix,

$$\begin{cases} S_{q+\Delta q+\Delta}^{-1} = \coth \theta \\ S_{qq+\Delta}^{-1} = (-1)^\Delta \coth \theta e^{-\Delta\theta} \end{cases}, \quad \Delta = 0, 1, 2, \dots, \quad (28)$$

with $S_{qq+\Delta}^{-1} = S_{q+\Delta q}^{-1}$. With the formulas of (28), we find the form of $\mathbf{S}_*^{-\frac{1}{2}}$,

$$\begin{aligned} \mathbf{S}_*^{-\frac{1}{2}} &= \begin{pmatrix} S_{qq}^{-1} & S_{qq+1}^{-1} \\ S_{qq+1}^{-1} & S_{q+1q+1}^{-1} \end{pmatrix}^{-\frac{1}{2}} \\ &= \begin{pmatrix} \coth \theta & -\coth \theta e^{-\theta} \\ -\coth \theta e^{-\theta} & \coth \theta \end{pmatrix}^{-\frac{1}{2}} \\ &= \frac{1}{2\sqrt{\coth \theta}} \begin{pmatrix} \alpha_- + \alpha_+ & \alpha_- - \alpha_+ \\ \alpha_- - \alpha_+ & \alpha_- + \alpha_+ \end{pmatrix}, \end{aligned} \quad (29)$$

with $\alpha_\pm = \frac{1}{\sqrt{1 \pm e^{-\theta}}}$. Combining (8) and (29), we write the orthogonal two-state basis $\{|\tilde{\varphi}_q\rangle, |\tilde{\varphi}_{q+1}\rangle\}$ as

$$\begin{aligned} |\tilde{\varphi}_q\rangle &= \sum_{j=q}^{q+1} S_{*,qj}^{-\frac{1}{2}} |\text{Loc}, j^*\rangle \\ &= \sum_{j=q}^{q+1} \sum_l S_{*,qj}^{-\frac{1}{2}} S_{jl}^{-1} |\text{Loc}, l\rangle, \end{aligned} \quad (30)$$

$$\begin{aligned} |\tilde{\varphi}_{q+1}\rangle &= \sum_{j=q}^{q+1} S_{*,q+1j}^{-\frac{1}{2}} |\text{Loc}, j^*\rangle \\ &= \sum_{j=q}^{q+1} \sum_l S_{*,q+1j}^{-\frac{1}{2}} S_{jl}^{-1} |\text{Loc}, l\rangle. \end{aligned} \quad (31)$$

In turn, the impurity matrix is constructed from (26) as

$$\mathbf{V}_{FB} = \begin{pmatrix} V_{*,qq} & V_{*,qq+1} \\ V_{*,q+1q} & V_{*,q+1q+1} \end{pmatrix}, \quad (32)$$

with $V_{*,nm} = \langle \text{Loc}, n^* | \hat{V}_{FB} | \text{Loc}, m^* \rangle$ and

(10), the effective impurity matrix is computed from (28), (29) and (32) and yields

flux-dependent energies $E_\pm = E_\pm(\phi)$ (which will be re-

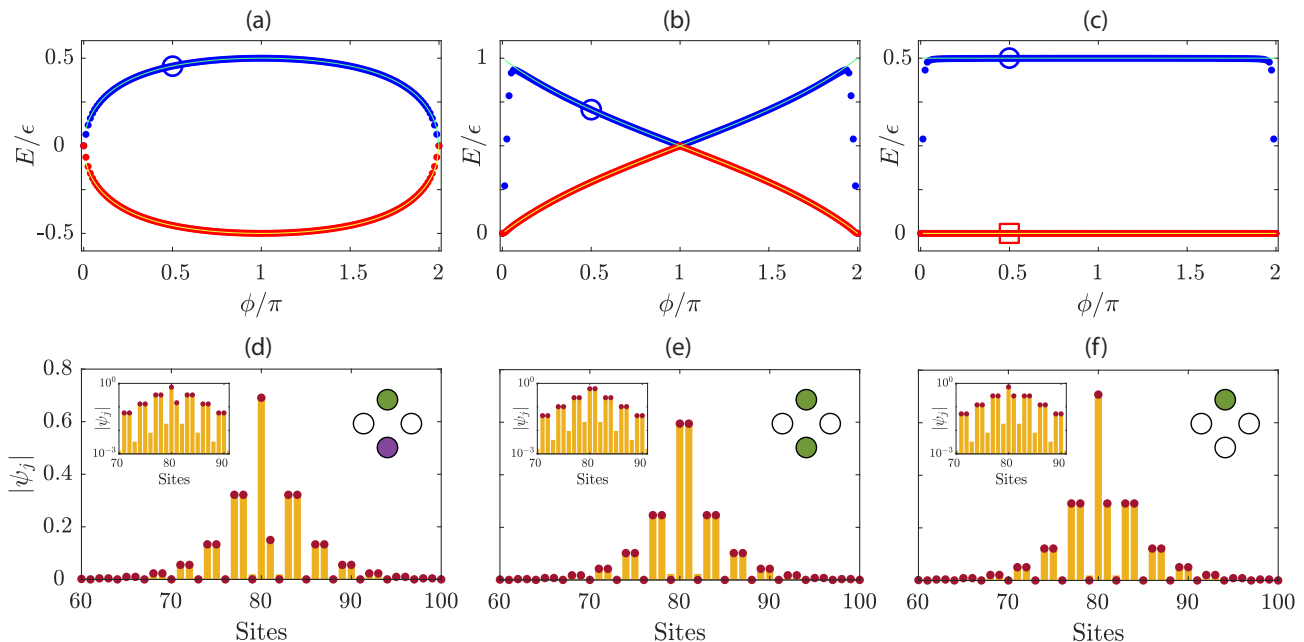


Figure 2. Analytical energy curves (light blue and yellow curves) obtained from diagonalization of the effective two-state system in (35), as a function of the magnetic flux ϕ for (a) symmetric impurities $\epsilon_B = -\epsilon_C = \epsilon$, (b) equal impurities $\epsilon_B = \epsilon_C = \epsilon$, and (c) a single impurity, $\epsilon_B = \epsilon$ and $\epsilon_C = 0$. Blue and red dots correspond to the numerically obtained energies of the two states of the FB that are affected by the impurity, for an open diamond chain with 53 plaquettes pierced by a ϕ flux, with the impurities placed at the B and C sites of the midchain plaquette in (a) and (b), and at its B site in (c). Note that the overlap between analytical curves and numerical dots renders the former invisible for most of the spectrum in all three cases. (d)-(f) Probability amplitudes of the eigenstate marked by a blue circle in the corresponding cases above. Only the central part of the chain is shown. Golden bars (red dots) correspond to numerical (analytical) results. The left insets plot the same results in a semi-logarithmic scale and for a smaller portion of the chain. Sites without red dots are A sites where the CLSs forming the analytical subspace have zero weight. The right insets depict the impurities at the midchain plaquette, with green (purple) color indicating an ϵ ($-\epsilon$) value for the impurity at that site. The blue circle (red square) in (c) also corresponds to the state shown on the top (bottom) of Fig. 5.

ferred hereafter as the “energy bands”, with the flux taking the place of a synthetic momentum) of the two states $|\tilde{\varphi}_\pm\rangle = |\tilde{\varphi}_\pm(\phi)\rangle$ within the zero-energy FB that are affected by the impurities at the $q+1$ plaquette, which are determined as

$$\begin{pmatrix} |\tilde{\varphi}_+\rangle \\ |\tilde{\varphi}_-\rangle \end{pmatrix} = \mathbf{U} \begin{pmatrix} |\tilde{\varphi}_q\rangle \\ |\tilde{\varphi}_{q+1}\rangle \end{pmatrix}, \quad (36)$$

where \mathbf{U} is the unitary matrix with eigenvectors as its rows, with elements $[U]_{ij} \equiv U_{ij}$, where $i, j = q, q+1$. Using (30)-(31), we can express $|\tilde{\varphi}_\pm\rangle$ in terms of the original CLSs,

$$|\tilde{\varphi}_+\rangle = \sum_{j=q}^{q+1} \sum_l [U_{qq} S_{*,qj}^{-\frac{1}{2}} + U_{qq+1} S_{*,q+1j}^{-\frac{1}{2}}] S_{jl}^{-1} |\text{Loc}, l\rangle, \quad (37)$$

$$|\tilde{\varphi}_-\rangle = \sum_{j=q}^{q+1} \sum_l [U_{q+1q} S_{*,qj}^{-\frac{1}{2}} + U_{q+1q+1} S_{*,q+1j}^{-\frac{1}{2}}] S_{jl}^{-1} |\text{Loc}, l\rangle. \quad (38)$$

Let us address separately three representative choices for the ϵ_B, ϵ_C local impurities shown in the right insets of Fig. 2(d)-(f) and analyze their solutions.

A. Symmetric impurities ($\epsilon_B = -\epsilon_C = \epsilon$)

For symmetric impurities, $\epsilon_B = -\epsilon_C = \epsilon$, where the impurity strength ϵ is given in units of the hopping parameter t , the effective impurity matrix in (35) reduces to

$$\tilde{\mathbf{V}}_{FB} = -\frac{\epsilon}{2} \sqrt{1 - e^{-2\theta}} \sigma_y, \quad (39)$$

with σ_μ ($\mu = x, y, z$) the μ Pauli matrix. The respective eigenvalues and eigenvectors read as

$$E_\pm = \pm \frac{\epsilon}{2} \sqrt{1 - e^{-2\theta}}, \quad (40)$$

$$\begin{pmatrix} |\tilde{\varphi}_+\rangle \\ |\tilde{\varphi}_-\rangle \end{pmatrix} = \frac{1}{\sqrt{2}} \begin{pmatrix} i & 1 \\ -i & 1 \end{pmatrix} \begin{pmatrix} |\tilde{\varphi}_q\rangle \\ |\tilde{\varphi}_{q+1}\rangle \end{pmatrix}. \quad (41)$$

In Fig. 2(a), we compare the analytical energies of (40) with numerical results as a function of the magnetic flux, for a chain with 53 plaquettes and symmetric local impurities at the top and bottom sites of the midchain plaquette [depicted in the right inset of Fig. 2(d)]. Two states with symmetric energies are lifted from the flat band for a finite magnetic flux per plaquette. Even though the

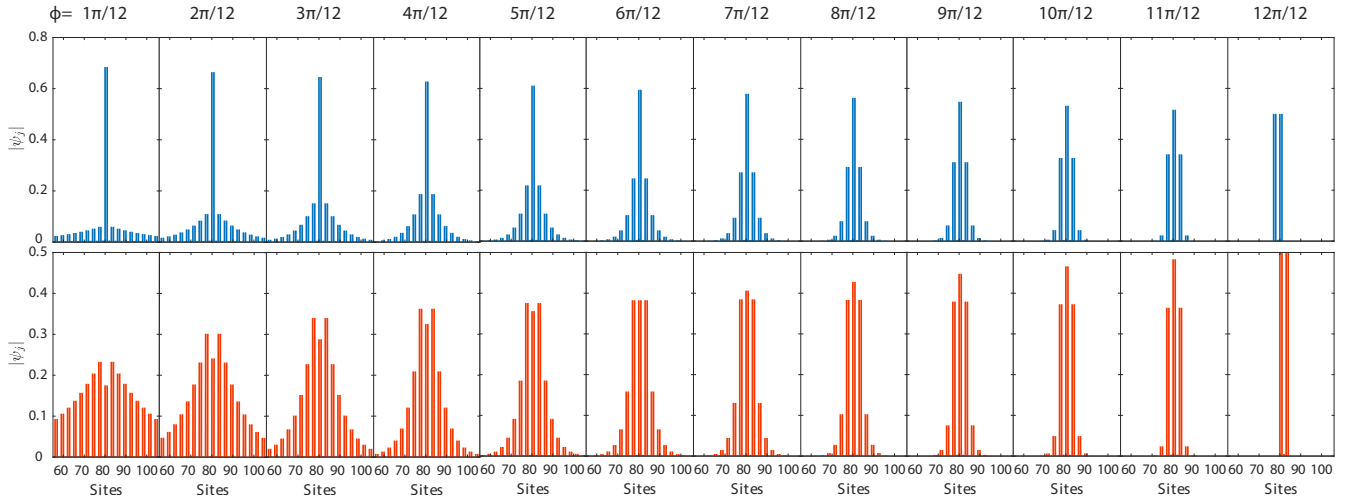


Figure 3. Snapshots of the amplitudes of the higher (lower) impurity state at the top (bottom) panel at different flux values, indicated on top, for a partial section of an open diamond chain with 53 complete plaquettes, with equal impurities $\epsilon = 0.1$ in the middle one. The energy of both states at each flux value is given in Fig. 2(b).

perturbation is already quite large, $\epsilon = 0.1$, that is, away for all ϕ from the $\epsilon \ll E_{\text{gap}}$ condition assumed in the projection of the impurity operator onto the flat band in (25), there is a nearly perfect match between analytical and numerical curves for the entire spectrum.

In Fig. 2(d), we plot the spatial profile of the eigenstate corresponding to the encircled positive energy at $\phi = \frac{\pi}{2}$ in Fig. 2(a). The analytical amplitude at each site, depicted as red dots, was computed by applying the general expression in (37), with the \mathbf{U} matrix for the symmetric impurities case given in (41), and agrees very well with the numerical one, represented by the golden bar at the corresponding site. The inset shows the same results but in a semi-logarithmic scale. Sites without red dots correspond to A sites where the localized states have zero weight, according to (15)-(16). The negligible numerical weight at these sites comes from higher-order terms that couple the perturbed states with the top and bottom dispersive bands.

B. Equal impurities ($\epsilon_B = \epsilon_C = \epsilon$)

For equal impurities, $\epsilon_B = \epsilon_C = \epsilon$, the effective impurity matrix in (35) reduces to

$$\tilde{\mathbf{V}}_{FB} = \frac{\epsilon}{2}(\sigma_0 + e^{-\theta}\sigma_x), \quad (42)$$

where σ_0 is the 2×2 identity matrix. The respective eigenvalues and eigenvectors read as

$$E_{\pm} = \frac{\epsilon}{2}(1 \pm e^{-\theta}), \quad (43)$$

$$\begin{pmatrix} |\tilde{\varphi}_+\rangle \\ |\tilde{\varphi}_-\rangle \end{pmatrix} = \frac{1}{\sqrt{2}} \begin{pmatrix} 1 & 1 \\ 1 & -1 \end{pmatrix} \begin{pmatrix} |\tilde{\varphi}_q\rangle \\ |\tilde{\varphi}_{q+1}\rangle \end{pmatrix}. \quad (44)$$

In Fig. 2(b), we compare the analytical energies of (43) with numerical results as a function of the magnetic flux

for the impurity distribution depicted in the right inset of Fig. 2(e). Two positive energy states are lifted from the FB for a finite magnetic flux per plaquette, and become degenerate with $E = 0.5\epsilon$ at $\phi = \pi$. Since $E_{\text{gap}} \rightarrow 0$ when $\phi \rightarrow 0 \pmod{2\pi}$, near the edges of the spectrum higher-order couplings to the dispersive bands can no longer be safely neglected, and the analytical treatment breaks down in that region. However, this region is still very small for $\epsilon = 0.1$, and shrinks even further with decreasing ϵ . The spatial amplitudes of the eigenstate with the energy marked by the blue circle in Fig. 2(b) are depicted in Fig. 2(e). As for the symmetric case above, a very good agreement is found between the numerical and analytical results.

1. Disorder

The localization length of the impurity states is controlled by the flux, as illustrated in Fig. 3. Having established numerically the validity of the analytical solutions considerably away from the $\epsilon \ll 1$ limit assumed in their derivation (the impurity strength is $\epsilon = 0.1$ in Fig. 2, and even higher values still yield good agreement with numerical results), one can study the effect of small disorder on the impurity states. More specifically, we will consider diagonal disorder on an open diamond chain with 101 plaquettes threaded by a ϕ flux, by setting the onsite potential at each site to a random value taken from a uniform distribution in the interval $[-\frac{\delta}{2}, \frac{\delta}{2}]$, with $\delta = 0.02$ the disorder strength, with a standard deviation given by $\sigma_{\text{ud}} = \frac{\delta}{\sqrt{12}} \approx 5.8 \times 10^{-3}$. For the sites at the mid-chain plaquette hosting the impurities, the disorder is added on top of $\epsilon = 0.1$. We perform 20000 disorder realizations for each flux value and track the energies of the impurity states, from where we construct their re-

spective histograms, as exemplified for the higher one at $\phi = \frac{9\pi}{20}$ in the inset of Fig. 4(b). Remarkably, the underlying uniform distribution of the disorder generates a normal distribution for the energies of the impurity states, whose mean approaches their disorder-free values given in Fig. 2(b) with increasing disorder realizations. This result is consistent with the central limit theorem (CLT), *i.e.*, for each realization the impurity states effectively feel an *averaged disorder* related to their localization length, that is, to their spatial extension.

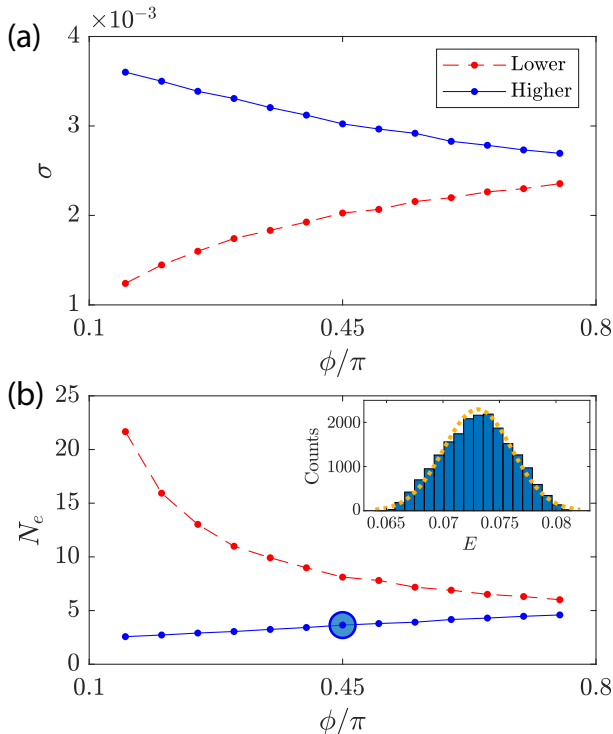


Figure 4. (a) Standard deviation, as a function of the flux, of the energy of both impurity states for an open diamond chain with 101 plaquettes, with equal impurities $\epsilon = 0.1$ in the middle one, taken from 20000 realizations of diagonal disorder at each point, with disorder strength $\delta = 0.02$. (b) Effective number of sites involved in the disorder averaging effect, computed from the corresponding standard deviation values in (a) in accordance with the CLT. The inset shows the energy histogram for the encircled higher-energy state at $\phi = 0.45\pi$, with the dashed orange curve corresponding to the Gaussian fit from which the standard deviation is extracted.

In Fig. 4(a), we plot the standard deviation of the Gaussian fit of the energy distributions of both impurity states as a function of the flux. The flux was taken in $\frac{\pi}{20}$ increments and restricted to the $[\frac{3\pi}{20}, \frac{15\pi}{20}]$ interval, since near $\phi = 0, \pi$ the energy separation of the states is of the order of δ [see numerical results in Fig. 2(b) in these regions], which leads to a reordering of the states and to an overlap of their corresponding energy distributions, preventing their independent analysis. According to the CLT, the standard deviation of the normal distribution is related to the sample size, which in our

case corresponds to the effective number of sites N_e over which the disorder is averaged for each impurity state, through $\sigma = \frac{\sigma_{ud}}{\sqrt{N_e}}$, with σ_{ud} given above. With this formula, and from the σ values given in Fig. 4(a), we plot in Fig. 4(b) the flux dependence of N_e for both impurity states. Interestingly, it can be seen that they follow opposite tendencies with increasing flux: while N_e decreases exponentially for the lower state, it increases monotonously for the higher state.

The evolution of the spatial profile of the impurity states with flux, shown in Fig. 3, can be used to explain their different response to disorder. The lower state becomes globally more and more localized until it becomes a CLS at $\phi = \pi$, which agrees with its decreasing N_e in Fig. 4(b), since the disorder is being averaged over fewer sites, therefore generating a higher effective onsite disorder on the lower state. The higher state, on the other hand, has dominant contributions from the impurity sites at lower fluxes (see central peaks in the top panel of Fig. 3 with growing weight for decreasing flux). The weights at these sites are in an anti-symmetric configuration that becomes the full eigenstate (a CLS) at $\phi = 0$, while they are in a symmetric configuration for the lower state. At zero flux, applying the same rotation to the B and C sites at each plaquette has been shown to decouple the anti-symmetric state, while the symmetric one connects with adjacent A sites to form a uniform chain [40]. As flux is increased, the anti-symmetric configuration of impurity sites couples to the uniform chain with growing strength [41] and, as with the lower state, the higher state develops a spatially extended profile that becomes increasingly localized (see the evolution of the components at sites other than the central impurity ones in the top panel of Fig. 3). Conversely, the peaks at the impurity sites, which are the main contributors to the number of effective sites N_e of the averaged disorder, continuously decrease with increasing flux, that is, spread their weight to the other sites. This effect, which tends to increase N_e , overpowers the localization effect of the other components, which tends to decrease N_e (as for the lower state), leading to the net increase of N_e with flux seen in Fig. 4(b).

While the normal distribution of the sample means expected from CLT is only exact, strictly speaking, in the limit of infinite sample size, $N_e \rightarrow \infty$, we have checked numerically that a Gaussian fit is in very good agreement with the energy histogram of all points in Fig. 4(b), including for the higher state, as exemplified in the inset, where the effective number of sites responsible for the averaged disorder is small, ranging from $N_e \approx 2.5$ to $N_e \approx 5$.

The averaging of diagonal disorder on the impurity states, conjectured to be the mechanism behind the enhanced robustness to disorder displayed by certain domain wall states with similar localization properties [42], is quantitatively confirmed here by the numerical results of Fig. 4. For the equal impurities case studied in this section, this enhanced robustness to disorder is greater for

the lower impurity state at low flux values where, according to Fig. 4(b), N_e is maximized. This is demonstrated in a follow up paper, where the response to disorder of effective systems of coupled impurity states is analyzed in greater detail [43].

C. Single impurity ($\epsilon_B = \epsilon, \epsilon_C = 0$)

Finally, let us address the case where a single impurity, $\epsilon_B = \epsilon$, is placed at the top site of the $q + 1$ plaquette. The effective impurity matrix in (35) reduces now to

$$\tilde{\mathbf{V}}_{FB} = \frac{\epsilon}{4}(\sigma_0 + e^{-\theta}\sigma_x - \sqrt{1 - e^{-2\theta}}\sigma_y). \quad (45)$$

The respective eigenvalues and eigenvectors read as

$$E_{\pm} = \frac{\epsilon}{4}(1 \pm 1), \quad (46)$$

$$\begin{pmatrix} |\tilde{\varphi}_+\rangle \\ |\tilde{\varphi}_-\rangle \end{pmatrix} = \frac{1}{\sqrt{2}} \begin{pmatrix} 1 & e^{-i\vartheta} \\ 1 & -e^{-i\vartheta} \end{pmatrix} \begin{pmatrix} |\tilde{\varphi}_q\rangle \\ |\tilde{\varphi}_{q+1}\rangle \end{pmatrix}, \quad (47)$$

$$\cos \vartheta := e^{-\theta} = \text{Exp} \left[-\cosh^{-1} \left[\sec \frac{\phi}{2} \right] \right], \quad (48)$$

where the formula for θ given in (21) was used in the last line. Both energy bands are flat and, in particular, we have $E_- = 0$, as shown in Fig. 2(c), meaning that, when a single impurity is present, the system can always rotate the subspace of dual localized states in order to generate a state, namely $|\tilde{\varphi}_-\rangle$ in (47), with zero weight at the impurity site, $\langle B_{q+1} | \tilde{\varphi}_-\rangle = 0$, such that it remains degenerate with the other FB states. This is illustrated in Fig. 5, where a partial profile of the $|\tilde{\varphi}_+\rangle$ and $|\tilde{\varphi}_-\rangle$ eigenstates, computed through (47) for $\phi = \frac{\pi}{2}$, is depicted [the complete profile of $|\tilde{\varphi}_+\rangle$ is shown in Fig. 2(f), which agrees very well with numerics]. It can be seen that the weight of the state at the impurity site is maximum for $|\tilde{\varphi}_+\rangle$ and zero for $|\tilde{\varphi}_-\rangle$.

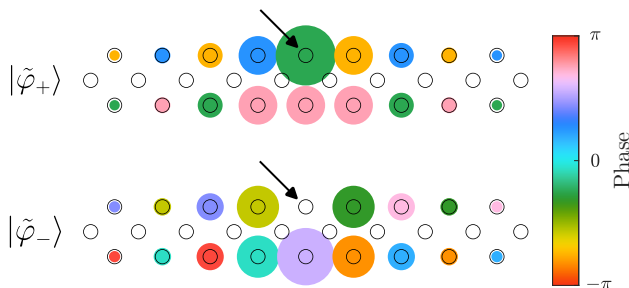


Figure 5. Partial profile of the $|\tilde{\varphi}_+\rangle$ and $|\tilde{\varphi}_-\rangle$ eigenstates with energies marked with a blue circle and a red square in Fig. 2(c), respectively, and where the radius of each circle represents the amplitude of the wavefunction at the respective site and the color represents its phase, coded by the color bar at the right. The arrow indicates the B_{q+1} site where the $\epsilon_B = \epsilon = 0.1$ impurity is placed, and where $|\tilde{\varphi}_+\rangle$ ($|\tilde{\varphi}_-\rangle$) has maximum (zero) amplitude.

1. Topological characterization

The topological characterization of the single-impurity case reveals interesting new features. Let us first summarize the usual approach to the topological characterization of gapped 1D two-band models. The relevant topological invariant for characterizing the energy gap is the Zak phase of the lower band, which can be expressed as

$$\gamma = i \oint dR \langle \tilde{\varphi}(R)_- | \frac{d}{dR} | \tilde{\varphi}(R)_- \rangle, \quad (49)$$

where the integral traces a closed path along the dimensional parameter R . For the textbook Su-Schrieffer-Heeger (SSH) two-band model [44], consisting of a chain with staggered hopping terms t_1 and t_2 , with the former (latter) corresponding to the intracell (intercell) hopping parameter [45], the lowest energy bulk eigenstate has the same form of $|\tilde{\varphi}_-\rangle$ in (47) when written in its site state basis, $|\tilde{\varphi}_-(k)\rangle = 1/\sqrt{2}(1, -e^{-i\vartheta(k)})^T$, where k is the momentum and $\cos \vartheta(k) = \frac{t_1}{t_2 \sin k} + \cot k$ [38, 46]. Inserting $|\tilde{\varphi}_-(k)\rangle$ in (49), where $R = k$ and the integral goes over the Brillouin zone (BZ), we get

$$\gamma = \frac{1}{2} \int_{\vartheta(0)}^{\vartheta(2\pi)} d\vartheta(k) = \frac{\Delta\vartheta}{2}, \quad (50)$$

with $\Delta\vartheta = \vartheta(2\pi) - \vartheta(0)$ yielding the total change in the $\vartheta(k)$ phase around the BZ. From the profile of $\vartheta(k)$ shown in Fig. 6, which has been experimentally confirmed recently in different platforms [47, 48], one readily obtains $\gamma = 0(\pi)$ for the (non-)trivial phase. According to the bulk-boundary correspondence, an open SSH chain will have zero edge states in the trivial $\gamma = 0$ phase, and two edge states in the non-trivial $\gamma = \pi$ phase, exponentially localized at opposite ends of the chain (up to hybridization effects stemming from finite size corrections).

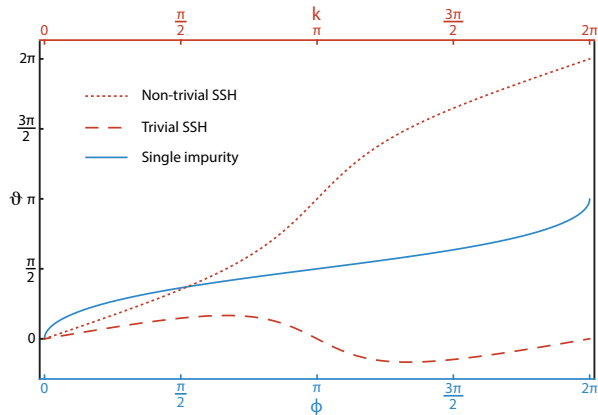


Figure 6. Phase ϑ of the lowest energy eigenstate as a function of the magnetic flux ϕ (momentum k) for the single-impurity model (SSH model). The color of each curve matches the color of the corresponding horizontal axis. For the SSH model, the ratio $t_1/t_2 = 2$ ($t_1/t_2 = 0.5$) was used for the topologically (non-)trivial case.

Let us turn our attention to the single-impurity case, with the gapped effective two-band spectrum given by the solid curves in Fig. 2(c). It is clear that the relevant parameter of integration is now, not the momentum k , but rather the reduced magnetic flux ϕ , as it changes by one flux quantum, that is, from $\phi = 0$ to $\phi = 2\pi$. By inserting $|\tilde{\varphi}_-\rangle = |\tilde{\varphi}_-(\phi)\rangle$, given in (47), in (49) leads to (50) with $k \rightarrow \phi$. Therefore, the Zak phase depends on the total variation of $\vartheta(\phi)$ in (48) over one flux quantum. The blue solid curve in Fig. 6 shows that $\Delta\vartheta = \pi$, leading to a Zak phase π -quantized to a *half-integer* value, $\gamma = \frac{\pi}{2}$. Alternatively, after rewriting the effective impurity matrix in (45) as

$$\tilde{\mathbf{V}}_{FB} = \frac{\epsilon}{4}\sigma_0 + \begin{pmatrix} 0 & h(\phi) \\ h^*(\phi) & 0 \end{pmatrix}, \quad (51)$$

where $h(\phi) = \frac{\epsilon}{4}e^{i\vartheta(\phi)}$, one can compute the winding number [45, 49] as

$$W = \frac{1}{2\pi i} \int_0^{2\pi} d\phi \frac{d}{d\phi} \log h(\phi) = \frac{\Delta\vartheta}{2\pi} = \frac{\gamma}{\pi} = \frac{1}{2}, \quad (52)$$

which similarly produces a half-integer value, meaning that ϕ needs to change adiabatically by two full cycles to produce one complete winding of $h(\phi)$ around the origin in the complex plane. Furthermore, from Fig. 6 and the form of the eigenvectors in (47), it can be seen that they are 4π -periodic in ϕ [since both energy bands are flat, see (46), the 4π -periodicity is not explicitly manifested there], and also that the eigenvectors exchange in multiples of 2π as

$$|\tilde{\varphi}_\pm(\phi)\rangle = |\tilde{\varphi}_\mp(\phi + 2\pi)\rangle = |\tilde{\varphi}_\pm(\phi + 4\pi)\rangle. \quad (53)$$

This behavior is remarkably similar to that observed in chiral-symmetric non-Hermitian 1D models where, due

to the fact that each exceptional point (EP) [50] carries a topological charge of $\pm 1/2$, the absolute value of the winding number, $|W|$, corresponds to half the number of times each EP is encircled as the momentum k traverses the BZ (assuming the wrapping around all EPs follows the same circulation, such that all individual contributions to W have the same sign). In particular, if a single EP is encircled once then one has $|W| = 1/2$ [51–53] and, analogously, the eigenstates of both bands (assuming a two-band model) are also exchanged after traversing the BZ [51, 54]. This non-Hermitian $|W| = 1/2$ case has been associated with the presence of a single edge state under open boundary conditions (OBC), and each $1/2$ increment in $|W|$ has been further associated with the appearance of an extra edge state [55]. Concerning the effective model for the single-impurity case studied in this section, it corresponds, to the best of our knowledge, to the first example of a Hermitian model with a half-integer winding number.

Regarding the Zak phase, on the other hand, the other known example of a 1D Hermitian model where it yields a half-integer value at its energy gaps is the diamond chain with π -flux per plaquette [19, 21] [where W is not well-defined since the off-diagonal block of the Hamiltonian in its chiral representation, corresponding here to the scalar $h(\phi)$ in (51), is not a square matrix]. The $\gamma = \frac{\pi}{2}$ value for the finite-energy bands of this model is a consequence of having a noncentered inversion-axis within the unit cell [56], such that the inversion operator picks up a k -dependence over one of the sublattices. Accordingly, a modified bulk-boundary correspondence is manifested by this system, one that matches a half-quantized Zak phase at a given energy gap with the presence of a *single* edge state at that gap, when open boundaries are considered [16, 17, 19, 21].

From the examples mentioned above, the same pattern seems to emerge both for Hermitian and non-Hermitian models, namely that a half-integer bulk topological invariant is connected to the presence of a single edge state under OBC. The question now becomes: given that the same half-integer invariants (winding number and Zak phase) are observed for our single-impurity case, is there a physical signature of this non-trivial behavior? Recall that the “bulk” bands in Fig. 2(c) are defined over the reduced flux ϕ , and not over a momentum variable k . Therefore, the concept of OBC does not directly apply here [57]. To circumvent this limitation, we adopt a strategy based on an *exact* mapping as follows. First, we consider the modified Lieb lattice depicted in Fig. 7(a), with a line of impurity sites at every other site along the y -direction (red sites), positioned at the center of the x coordinate. Then, assuming PBC (OBC) in the y -direction (x -direction), we Fourier transform the lattice along the y -direction (with lattice constant set to unity) using the supercell represented in Fig. 7(a), obtaining the open diamond chain in Fig. 7(b). As a result, this chain becomes the same as the single-impurity case of Fig. 1(a), with k_y taking the place of ϕ , and up to an

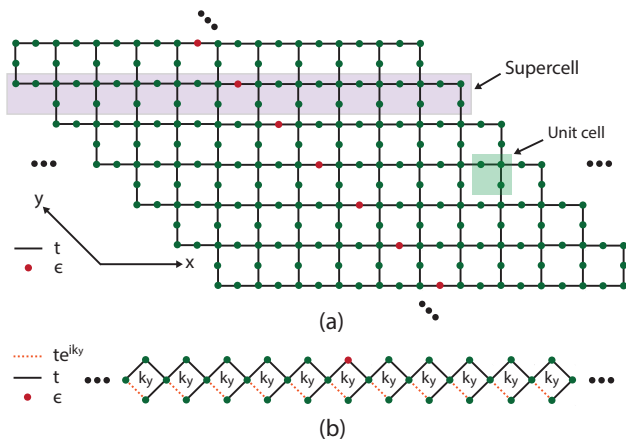


Figure 7. (a) Lieb lattice with a mid-length line of onsite impurity potentials ϵ at every other site (red dots) along the y -direction. All hopping terms are given by t . (b) Diamond chain obtained from Fourier transforming the lattice in (a) along the periodic y -direction, using the indicated supercell. The y -momentum k_y becomes the equivalent of a flux per plaquette. The dashed hoppings pick up a positive k_y phase in the clockwise direction within each plaquette.

inconsequential gauge transformation that accumulates all the k_y “flux” in a single hopping term within each plaquette. Therefore, for a small value of ϵ we expect the effective low-energy subspace to behave as in Fig. 2(c), with $\phi \rightarrow k_y$. The same half integer invariants γ and W in (50) and (52), respectively, are obtained when integrating now over the Brillouin zone in k_y . In order to test if this translates into the appearance of a gapped edge state in real-space, we impose OBC along the y -direction also, *i.e.*, we consider the Lieb lattice in Fig. 7(a) with OBC for both directions. In Fig. 8(a), we plot the energy spectrum for a chain $N_x = 41$ ($N_y = 200$) unit cells in the x (y) direction, with impurities $\epsilon = 0.1$ placed along unit cell 21 in x according to the pattern in Fig. 7(a). The overall features of the spectrum in Fig. 8(a) are the expected ones for a Lieb lattice, namely a gapless system of two continua of dispersive states above and below the localized states of the zero-energy flat band. However, a closer look at the states with energies around $0 \leq E \lesssim \frac{\epsilon}{2}$ [notice how these limits correspond to the energies of the flat bands of the effective system in Fig. 2(c)], shown in the zoomed region of Fig. 8(b), reveals the presence of an energy gap. As expected, an isolated edge state is seen to appear within this gap, with the spatial profile depicted in Fig. 8(c).

The presence of an energy gap was not guaranteed *a priori* since, loosely speaking, the spectrum sweeps all the k_y values allowed by the OBC, and the gap between the dispersive and flat bands closes as $k_y \rightarrow 0$ [58]. Moreover, contrary to the analytical results for the effective model, the numerical results of Fig. 2(c) also show that the gap between the two bands closes at the edges (see the descending blue dots tending towards the red ones near $\phi \rightarrow k_y = 0, 2\pi$). But since this gap closing region is very

sharp, getting narrower as $\epsilon \rightarrow 0$, few solutions are expected to appear in this region under OBC. Indeed, some states at the left edge of the top band in Fig. 8(b) are bending towards the zero-energy band, while nonetheless keeping close to the top flat band at $E = \frac{\epsilon}{2} = 0.05$, such that the gap remains open and the edge state fully gapped. In Fig. 8(d), we show the spatial profile of the leftmost state of this subset. It can be seen that, while consisting mostly of a bulk state along the impurity line, there is still a finite weight on the region of the right edge state, which gradually shrinks as the state index increases, eventually vanishing once the flat band states at $E = 0.05$ are reached [see the profile of the state in Fig. 8(e)]. We attribute the right edge component for this subset of states to a perturbative hybridization with the gapped edge state that further sharpens their energy bending.

The results of this exact mapping provide another example where the half-integer topological bulk invariants, $\gamma = \pi W = \frac{\pi}{2}$, have a correspondence with the presence of a single gapped edge state under OBC. In turn, this provides indirect evidence that the topologically non-trivial nature of the single-impurity case studied in this section can be related to specific physical manifestations. We note that this bulk-boundary correspondence should also be observed upon switching the single impurity from the B site of the midchain plaquette, as in Fig. 7(b), to its C site. In terms of the Lieb lattice in Fig. 7(a), this corresponds to shifting the impurities along the impurity line, exchanging its red and green sites. As we detail in Appendix A, this shift leads to a physically distinct configuration that produces small changes to the low-energy spectrum in Fig. 8(b). However, as we show there, the validity of this mapping is not affected, as a single in-gap state is still present.

V. CONCLUSIONS

We studied a diamond chain with a gapped FB in its energy spectrum upon introducing a finite magnetic flux per plaquette, whose states can be described as CLSs spanning a non-orthogonal basis subspace. After outlining the mathematical formalism required for the analytical treatment of such non-orthogonal bases, we applied it to the general solutions of the impurity states that are lifted from the FB by small local potentials placed at the midchain plaquette. For the two equal, two symmetric and single-impurity cases, the numerical results were shown to closely follow the analytical predictions, except for flux values very close to the critical gap closing point between flat and dispersive bands, corresponding to the expected breakdown region of the theory.

Disorder studies were conducted for the case of equal impurities. By applying small disorder following a uniform distribution to the diamond chain, the energy histogram of both impurity states was seen to follow a normal distribution for a wide range of flux values. These

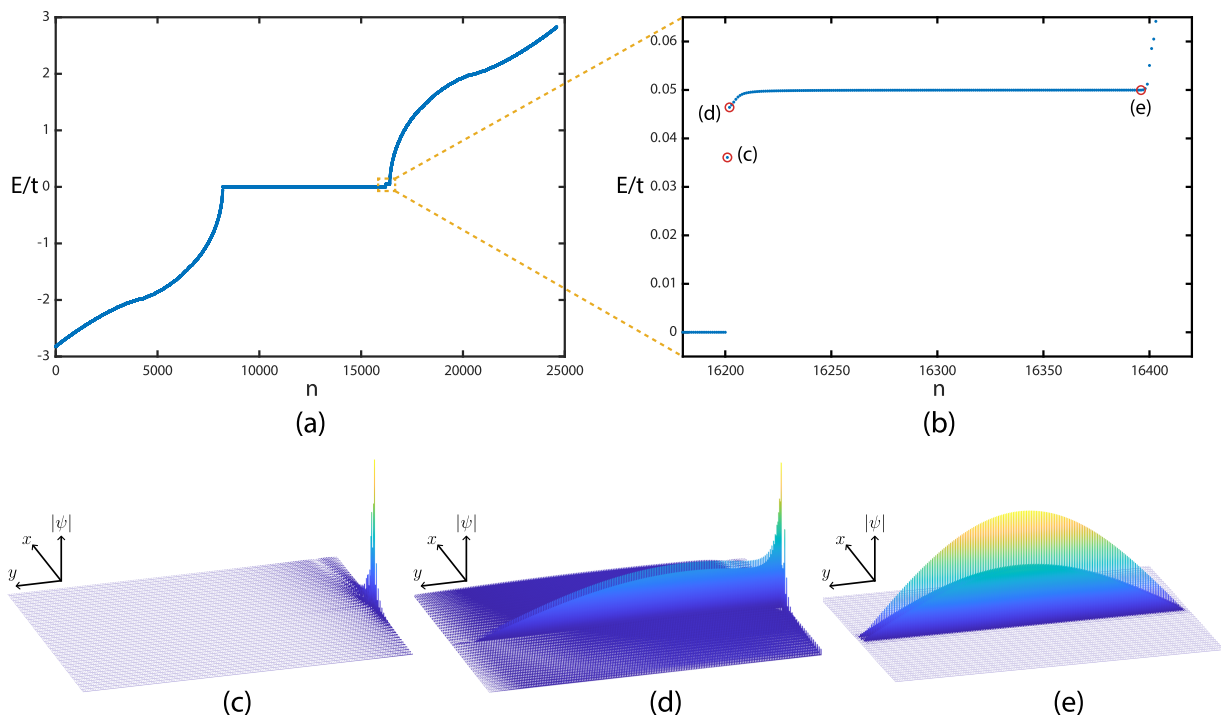


Figure 8. (a) Energy spectrum, with t as the energy unit, of the impurity decorated open Lieb lattice, with $N_x = 41$ ($N_y = 200$) unit cells in the x (y) direction and impurities $\epsilon = 0.1$ placed along unit cell 21 in x according to the pattern in Fig. 7(a). (b) Zoomed energy spectrum of the region delimited by the orange dashed box in (a). (c)-(e) Depiction of the amplitude distribution of the eigenstate with index (c) $n = 16201$, (d) $n = 16202$, and (e) $n = 16396$, with energies given by the corresponding encircled states in (b).

findings were connected to the CLT, such that, from relating the standard deviations of the normal and uniform distributions, an effective number of sites involved in a disorder averaging effect [42] was computed for each impurity state. We discussed how this effect translates into an enhanced robustness of the states to diagonal disorder, which is one of the most common kinds of disorder present in real systems.

A topological characterization of the impurity levels was carried out, where the flux was interpreted as a synthetic momentum. While the equal and symmetric impurity cases were characterized as topologically trivial, the single-impurity case manifested a peculiar type of non-trivial topology, namely one defined by half-integer invariants such as the Zak phase and winding number. The latter corresponds, as far as we know, to the first of its kind in the context of Hermitian models. Given that the invariants are computed by considering the reduced magnetic flux as the “bulk” variable of integration, and the variation of the flux by a flux quantum as the “Brillouin zone”, the bulk-boundary correspondence cannot be directly checked. However, an indirect way of circumventing this limitation was formulated, based on an exact mapping between the diamond chain with a single impurity and a two-dimensional Lieb lattice with a central line of impurities. The mapped lattice displays the same low-energy effective impurity bulk bands, classified by the

same half-integer invariants. For fully open boundaries, its energy spectrum reveals the presence of a single edge state within the gap of this low-energy subspace, providing an indirect evidence of the unconventional bulk-boundary correspondence associated with the topology of the single-impurity case.

Regarding the realization of the model studied here, shown in Fig. 1(a), we highlight two platforms. One is electrical circuits [59], whose flexibility and plasticity allows one to recreate most tight-binding models simply by coupling nodes with capacitors or inductors in the desired geometry. By incorporating negative impedance converters with current inversion (INICs) [60, 61] in phase-control units, it has been shown [62] that arbitrary phase factors can be associated to the couplings, enabling the generation of a synthetic flux at each plaquette, as required by the target model of Fig. 1(a). The impurity potentials at the central nodes can be simulated by adding extra capacitors, with small capacitance values, to the grounding schemes of these nodes. Preliminary numerical studies should be undertaken to determine the optimal parameters of the circuit since, on the one hand, the admittance elements of the impurity nodes should be small, compared to the admittance gap between flat and dispersive bands, and, on the other hand, they should be sufficiently higher than the tolerance of the other components, so as to not have its effects washed away by this in-

herent disorder. As such, very low tolerance components should be considered. After feeding the circuit with an alternated current with the eigenfrequency of the impurity states, standard voltage and two-point impedance measurements can be used to detect them.

The other strong possibility consists in implementing the diamond chain in photonic lattices. Three different options can be considered: (i) photonic waveguide arrays, where the synthetic flux can be generated by an appropriate bending of the lattice along its longitudinal direction [15], while the impurity potentials are controlled by the index of refraction of the corresponding waveguides (which in turn depends on the difference in lasing speed that is used to write them [63]); (ii) microring resonator arrays, where the synthetic flux can be controlled by displacing or modifying the optical path of the auxiliary rings used to effectively couple the main ones [64–66], and the impurities can be introduced by locally perturbing the resonance condition of the main lattice rings [67] (through slightly modifying their size, width or refractive index); (iii) arrays of coupled multiorbital waveguides [20, 68–70] guiding staggered orbital angular momentum (OAM) modes of order $l = 0, \pm 1$ where, in analogy with systems of ultracold atoms [71–73], the synthetic flux can be produced by geometrical manipulation of the waveguide pattern of the excited OAM modes [74, 75], while local potentials can again be introduced via changes to their radii or refractive index.

Our work provides a conceptual frame within which future studies on systems with non-orthogonal bases can be carried out. In particular, we discuss in greater detail in a companion piece to this paper [43] how one can, using the implementation platform (iii) above, and by decorating the diamond chain with impurities placed at regular intervals, extract impurity subspaces realizing different effective models from the FB, including topological ones hosting edge states.

ACKNOWLEDGMENTS

A.M.M. and R.G.D. developed their work within the scope of the Portuguese Institute for Nanostructures, Nanomodelling, and Nanofabrication (i3N) Projects No. UIDB/50025/2020, No. UIDP/50025/2020, and No. LA/P/0037/2020, financed by national funds through the Fundação para a Ciência e Tecnologia (FCT) and the Ministério da Educação e Ciência (MEC) of Portugal. A.M.M. acknowledges financial support from i3N through the work Contract No. CDL-CTTRI-46-SGRH/2022. D.V. and V.A. acknowledge financial support from the Spanish State Research Agency AEI (contract No. PID2020-118153GBI00/AEI/10.13039/501100011033) and Generalitat de Catalunya (Contract No. SGR2021-00138).

Appendix A: Comments on the single-impurity case

The Hamiltonian of the diamond chain in Fig. 1(a) can be parametrized as $H = H(\phi, \epsilon_B, \epsilon_C)$. For the general case, a y -mirror quasi-symmetry, with the mirror axis going through all the spinal A sites, can be defined as

$$M_y H(\phi, \epsilon_B, \epsilon_C) M_y^{-1} = H(-\phi, \epsilon_C, \epsilon_B), \quad (\text{A1})$$

where M_y is the y -mirror operator. Under this quasi-symmetry, the flux is reversed and the impurities exchange their positions, such that it only becomes an exact symmetry for the equal impurities case $\epsilon_B = \epsilon_C$. On the other hand, under time-reversal, the system behaves as

$$K H(\phi, \epsilon_B, \epsilon_C) K^{-1} = H(-\phi, \epsilon_B, \epsilon_C), \quad (\text{A2})$$

where K is the conjugation operator obeying $KK^{-1} = 1$. The combination of y -mirror and time-reversal operations yields

$$K M_y H(\phi, \epsilon_B, \epsilon_C) M_y^{-1} K^{-1} = H(\phi, \epsilon_C, \epsilon_B). \quad (\text{A3})$$

For a general eigenstate $|\psi_n\rangle$ of H , the Schrödinger equation has the form

$$H(\phi, \epsilon_B, \epsilon_C) |\psi_n\rangle = E_n |\psi_n\rangle. \quad (\text{A4})$$

Applying $K M_y$ from the left to both sides of (A4) leads to

$$H(\phi, \epsilon_C, \epsilon_B) K M_y |\psi_n\rangle = E_n K M_y |\psi_n\rangle, \quad (\text{A5})$$

where (A3) was used. By defining $|\psi'_n\rangle := K M_y |\psi_n\rangle$, (A5) becomes

$$H(\phi, \epsilon_C, \epsilon_B) |\psi'_n\rangle = E_n |\psi'_n\rangle, \quad (\text{A6})$$

which, as could be expected, tells us that the energy spectrum is invariant under an exchange of the impurities.

Through the mapping developed for the single-impurity case in Sec. IVC, we arrived at the substitution $\phi \rightarrow k_y$. The corresponding combined quasi-symmetry acting on the diamond chain depicted in Fig. 7(b) becomes, from (A3), and up to a gauge transformation that redistributes the k_y “flux” equally between all hopping terms of each plaquette,

$$K M_y H(k_y, \epsilon, 0) M_y^{-1} K^{-1} = H(k_y, 0, \epsilon). \quad (\text{A7})$$

As shown in (A6), $H(k_y, \epsilon, 0)$ and $H(k_y, 0, \epsilon)$ are isospectral. However, when OBC are considered in the y -direction, and for an integer number of supercells, this isospectrality is lost due to the fact that placing the impurities at the B sites [as in Fig. 7(a)] or at the C sites [corresponding to exchanging the red and green sites along the impurity line in Fig. 7(a)] corresponds to two nonequivalent configurations. This can be understood as follows. When the clean, impurity-free lattice in Fig. 7(a) with PBC along the y -direction is considered, the y -mirror axis is shifted from the center of the

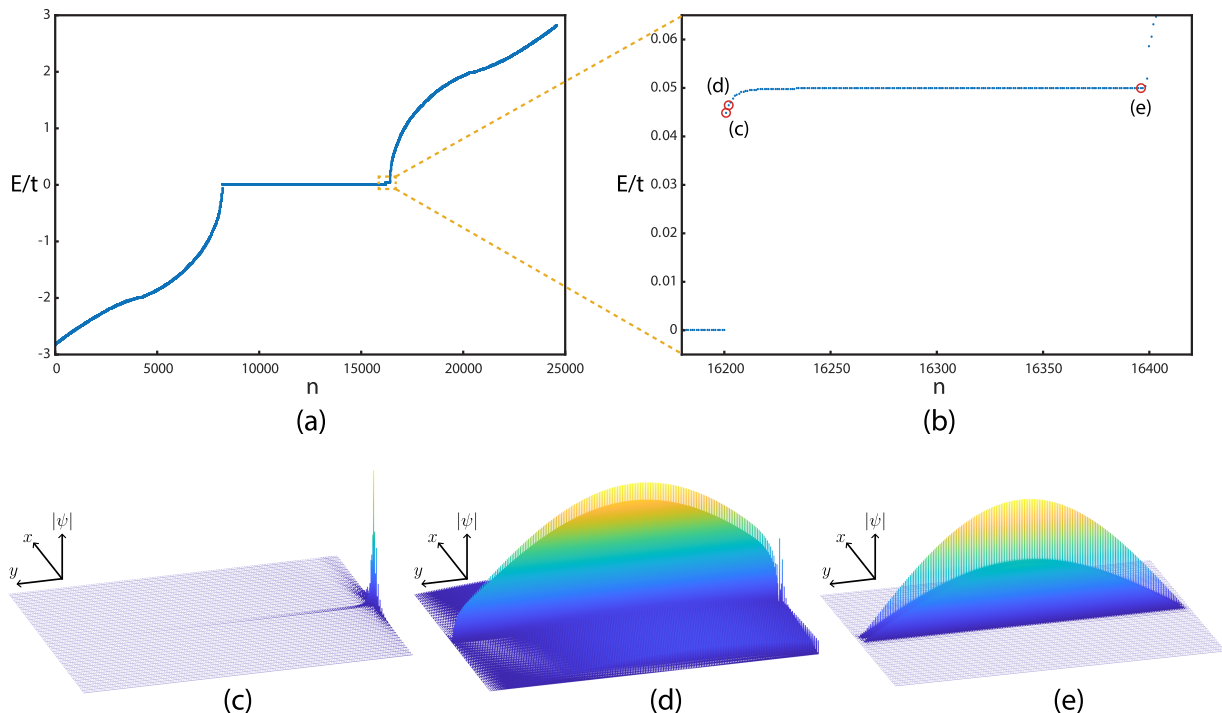


Figure 9. (a) Energy spectrum, with t as the energy unit, of the impurity decorated open Lieb lattice, with $N_x = 41$ ($N_y = 200$) unit cells in the x (y) direction and impurities $\epsilon = 0.1$ placed along unit cell 21 in x as in Fig. 7(a), but with every impurity shifted by one position along the impurity line (corresponding to exchanging the red and green sites along this line). (b) Zoomed energy spectrum of the region delimited by the orange dashed box in (a). (c)-(e) Depiction of the amplitude distribution of the eigenstate with index (c) $n = 16201$, (d) $n = 16202$, and (e) $n = 16396$, with energies given by the corresponding encircled states in (b).

supercell [56, 76], which induces a k_y -dependence in the y -mirror operator of the lattice [77]. More importantly, if OBC are now imposed along the y -direction, the lattice loses the y -mirror symmetry, since the top and bottom ends are different: from Fig. 7(a), it can be checked that, for OBC along the y -direction and an integer number of supercells, the top end is a horizontal line of sites, while the bottom end is composed of a horizontal sequence of dangling sites, thus breaking y -mirror symmetry (it can only be restored by adding extra sites from an incomplete supercell at one of the edges). This entails that, when the impurity line is included, the positioning of the impurities at the B or C sites leads to physically distinct configurations.

The question we want to address here is the following: when changing the impurities from the B sites along the impurity line, as in Fig. 7(a), to the C sites (by exchanging the red and green sites along this line), do the relevant qualitative features of the low-energy spectrum remain the same? In other words, does one still observe an energy gap between two flat or nearly-flat bands with a single in-gap edge state, as in Fig. 8(b), such that the

bulk-boundary correspondence is preserved, that is, is the system insensitive to the choice of impurity positioning? In Fig. 9, we replicate the energy spectrum of the same Lieb lattice with the spectrum of Fig. 8(a), apart from changing the position of the impurities to the C sites along the impurity line, following the procedure explained above. As can be seen in the zoomed low-energy spectrum of Fig. 9(b), a single in-gap state is found, albeit much closer in energy to the top bulk band than in Fig. 8(b). The spatial profile of this state is depicted in Fig. 8(c), confirming its edge localized nature. The energy state immediately above this one, depicted in Fig. 9(d), is confirmed to be a bulk state of the impurity line. Even though this first bulk state of the top band is closer to the in-gap state than in Fig. 8(b), a weaker hybridization with the edge state than for the state in Fig. 8(d) is observed. Finally, the last state of the top band is shown in Fig. 9(e), closely replicating the one in Fig. 8(e). In summary, while small quantitative differences are observed between the two choices of impurity positioning, both share the same qualitative features, most notably the presence of a single in-gap state in the relevant low-energy sector of the spectrum.

[1] S. Flach, D. Leykam, J. D. Bodyfelt, P. Matthies, and A. S. Desyatnikov, Detangling flat bands into fano lat-

tices, *Europphys Letters* **105**, 30001 (2014).

- [2] C. Danieli, A. Andreanov, D. Leykam, and S. Flach, Flat band fine-tuning and its photonic applications (2024), arXiv:2403.17578.
- [3] P. Sathe, F. Harper, and R. Roy, Compactly supported wannier functions and strictly local projectors, *Journal of Physics A: Mathematical and Theoretical* **54**, 335302 (2021).
- [4] P. Sathe and R. Roy, Compact wannier functions in one dimension (2024), arXiv:2302.11608.
- [5] W. Maimaiti, A. Andreanov, H. C. Park, O. Gendelman, and S. Flach, Compact localized states and flat-band generators in one dimension, *Phys. Rev. B* **95**, 115135 (2017).
- [6] W. Maimaiti, S. Flach, and A. Andreanov, Universal $d = 1$ flat band generator from compact localized states, *Phys. Rev. B* **99**, 125129 (2019).
- [7] R. G. Dias and J. D. Gouveia, Origami rules for the construction of localized eigenstates of the hubbard model in decorated lattices, *Scientific Reports* **5**, 16852 (2015).
- [8] W. Maimaiti, A. Andreanov, and S. Flach, Flat-band generator in two dimensions, *Phys. Rev. B* **103**, 165116 (2021).
- [9] Y. Hwang, J.-W. Rhim, and B.-J. Yang, General construction of flat bands with and without band crossings based on wave function singularity, *Phys. Rev. B* **104**, 085144 (2021).
- [10] A. Graf and F. Piéchon, Designing flat-band tight-binding models with tunable multifold band touching points, *Phys. Rev. B* **104**, 195128 (2021).
- [11] H. Kim, C.-g. Oh, and J.-W. Rhim, General construction scheme for geometrically nontrivial flat band models, *Communications Physics* **6**, 305 (2023).
- [12] C. Danieli, A. Andreanov, T. Mithun, and S. Flach, Nonlinear caging in all-bands-flat lattices, *Phys. Rev. B* **104**, 085131 (2021).
- [13] S. Li, Z.-Y. Xue, M. Gong, and Y. Hu, Non-abelian aharonov-bohm caging in photonic lattices, *Phys. Rev. A* **102**, 023524 (2020).
- [14] A. Mukherjee, A. Nandy, S. Sil, and A. Chakrabarti, Engineering topological phase transition and aharonov-bohm caging in a flux-staggered lattice, *Journal of Physics: Condensed Matter* **33**, 035502 (2020).
- [15] S. Mukherjee, M. Di Liberto, P. Öhberg, R. R. Thomson, and N. Goldman, Experimental observation of aharonov-bohm cages in photonic lattices, *Phys. Rev. Lett.* **121**, 075502 (2018).
- [16] G. Pelegrí, A. M. Marques, R. G. Dias, A. J. Daley, V. Ahufinger, and J. Mompart, Topological edge states with ultracold atoms carrying orbital angular momentum in a diamond chain, *Phys. Rev. A* **99**, 023612 (2019).
- [17] G. Pelegrí, A. M. Marques, R. G. Dias, A. J. Daley, J. Mompart, and V. Ahufinger, Topological edge states and aharonov-bohm caging with ultracold atoms carrying orbital angular momentum, *Phys. Rev. A* **99**, 023613 (2019).
- [18] M. Di Liberto, S. Mukherjee, and N. Goldman, Nonlinear dynamics of aharonov-bohm cages, *Phys. Rev. A* **100**, 043829 (2019).
- [19] M. Kremer, I. Petrides, E. Meyer, M. Heinrich, O. Zilberberg, and A. Szameit, A square-root topological insulator with non-quantized indices realized with photonic aharonov-bohm cages, *Nature Communications* **11**, 907 (2020).
- [20] G. Cáceres-Aravena, D. Guzmán-Silva, I. Salinas, and R. A. Vicencio, Controlled transport based on multi-orbital aharonov-bohm photonic caging, *Phys. Rev. Lett.* **128**, 256602 (2022).
- [21] A. M. Marques, L. Madail, and R. G. Dias, One-dimensional 2^n -root topological insulators and superconductors, *Phys. Rev. B* **103**, 235425 (2021).
- [22] A. M. Marques, J. Mögerle, G. Pelegrí, S. Flannigan, R. G. Dias, and A. J. Daley, Kaleidoscopes of hofstadter butterflies and aharonov-bohm caging from 2^n -root topology in decorated square lattices, *Phys. Rev. Res.* **5**, 023110 (2023).
- [23] T. Čadež, Y. Kim, A. Andreanov, and S. Flach, Metal-insulator transition in infinitesimally weakly disordered flat bands, *Phys. Rev. B* **104**, L180201 (2021).
- [24] Y. Kim, T. Čadež, A. Andreanov, and S. Flach, Flat band induced metal-insulator transitions for weak magnetic flux and spin-orbit disorder, *Phys. Rev. B* **107**, 174202 (2023).
- [25] Y. Kuno, T. Mizoguchi, and Y. Hatsugai, Interaction-induced doublons and embedded topological subspace in a complete flat-band system, *Phys. Rev. A* **102**, 063325 (2020).
- [26] G. Pelegrí, A. M. Marques, V. Ahufinger, J. Mompart, and R. G. Dias, Interaction-induced topological properties of two bosons in flat-band systems, *Phys. Rev. Research* **2**, 033267 (2020).
- [27] M. Tovmasyan, E. P. L. van Nieuwenburg, and S. D. Huber, Geometry-induced pair condensation, *Phys. Rev. B* **88**, 220510(R) (2013).
- [28] E. Nicolau, A. M. Marques, R. G. Dias, J. Mompart, and V. Ahufinger, Many-body aharonov-bohm caging in a lattice of rings, *Phys. Rev. A* **107**, 023305 (2023).
- [29] P.-O. Löwdin, Quantum theory of cohesive properties of solids, *Advances in Physics* **5**, 1 (1956).
- [30] M. Soriano and J. J. Palacios, Theory of projections with nonorthogonal basis sets: Partitioning techniques and effective hamiltonians, *Phys. Rev. B* **90**, 075128 (2014).
- [31] F. D. R. Santos and R. G. Dias, Methods for the construction of interacting many-body hamiltonians with compact localized states in geometrically frustrated clusters, *Scientific Reports* **10**, 4532 (2020).
- [32] D. V. Shalashilin and M. S. Child, The phase space ccs approach to quantum and semiclassical molecular dynamics for high-dimensional systems, *Chemical Physics* **304**, 103 (2004), towards Multidimensional Quantum Reaction Dynamics.
- [33] C. Symonds, J. Wu, M. Ronto, C. Zagoya, C. Figueira de Morisson Faria, and D. V. Shalashilin, Coupled-coherent-states approach for high-order harmonic generation, *Phys. Rev. A* **91**, 023427 (2015).
- [34] E. Schmidt, Zur theorie der linearen und nichtlinearen integralgleichungen, *Mathematische Annalen* **63**, 433 (1907).
- [35] Y. Leschber and J. P. Draayer, Orthogonal polynomial expansion for the lowdin transformation, *Journal of Physics A: Mathematical and General* **22**, 2675 (1989).
- [36] K. Suzuki, S. Maruyama, and K. Araki, Generalized method for calculating löwdin orbitals, *Bulletin of the Chemical Society of Japan* **46**, 355 (1973).
- [37] C. da Fonseca and J. Petronilho, Explicit inverses of some tridiagonal matrices, *Linear Algebra and its Applications* **325**, 7 (2001).
- [38] A. M. Marques and R. G. Dias, Analytical solution of

- open crystalline linear 1d tight-binding models, *Journal of Physics A: Mathematical and Theoretical* **53**, 075303 (2020).
- [39] A. A. Lopes, B. A. Z. António, and R. G. Dias, Conductance through geometrically frustrated itinerant electronic systems, *Phys. Rev. B* **89**, 235418 (2014).
- [40] E. Nicolau, A. M. Marques, J. Mompart, V. Ahufinger, and R. G. Dias, Local hilbert space fragmentation and weak thermalization in bose-hubbard diamond necklaces, *Phys. Rev. B* **107**, 094312 (2023).
- [41] A. A. Lopes and R. G. Dias, Interacting spinless fermions in a diamond chain, *Phys. Rev. B* **84**, 085124 (2011).
- [42] F. Munoz, F. Pinilla, J. Mella, and M. I. Molina, Topological properties of a bipartite lattice of domain wall states, *Scientific Reports* **8**, 17330 (2018).
- [43] D. Viedma, A. M. Marques, R. G. Dias, and V. Ahufinger, in preparation.
- [44] W. P. Su, J. R. Schrieffer, and A. J. Heeger, Solitons in polyacetylene, *Phys. Rev. Lett.* **42**, 1698 (1979).
- [45] J. K. Asbóth, L. Oroszlány, and A. Pályi, *A Short Course on Topological Insulators* (Springer, Berlin, 2016).
- [46] P. Delplace, D. Ullmo, and G. Montambaux, Zak phase and the existence of edge states in graphene, *Phys. Rev. B* **84**, 195452 (2011).
- [47] G. Li, L. Wang, R. Ye, Y. Zheng, D.-W. Wang, X.-J. Liu, A. Dutt, L. Yuan, and X. Chen, Direct extraction of topological zak phase with the synthetic dimension, *Light: Science & Applications* **12**, 81 (2023).
- [48] I. Neder, C. Sirote-Katz, M. Geva, Y. Lahini, R. Ilan, and Y. Shokef, Bloch oscillations, landau-zener transition, and topological phase evolution in an array of coupled pendula, *Proceedings of the National Academy of Sciences* **121**, e2310715121 (2024).
- [49] M. Maffei, A. Dauphin, F. Cardano, M. Lewenstein, and P. Massignan, Topological characterization of chiral models through their long time dynamics, *New Journal of Physics* **20**, 013023 (2018).
- [50] E. J. Bergholtz, J. C. Budich, and F. K. Kunst, Exceptional topology of non-hermitian systems, *Rev. Mod. Phys.* **93**, 015005 (2021).
- [51] T. E. Lee, Anomalous edge state in a non-hermitian lattice, *Phys. Rev. Lett.* **116**, 133903 (2016).
- [52] Ó. Viyuela, D. Vodola, G. Pupillo, and M. A. Martin-Delgado, Topological massive dirac edge modes and long-range superconducting hamiltonians, *Phys. Rev. B* **94**, 125121 (2016).
- [53] D. Leykam, K. Y. Bliokh, C. Huang, Y. D. Chong, and F. Nori, Edge modes, degeneracies, and topological numbers in non-hermitian systems, *Phys. Rev. Lett.* **118**, 040401 (2017).
- [54] H. Shen, B. Zhen, and L. Fu, Topological band theory for non-hermitian hamiltonians, *Phys. Rev. Lett.* **120**, 146402 (2018).
- [55] C. Yin, H. Jiang, L. Li, R. Lü, and S. Chen, Geometrical meaning of winding number and its characterization of topological phases in one-dimensional chiral non-hermitian systems, *Phys. Rev. A* **97**, 052115 (2018).
- [56] A. M. Marques and R. G. Dias, One-dimensional topological insulators with noncentered inversion symmetry axis, *Phys. Rev. B* **100**, 041104(R) (2019).
- [57] Note that the bulk-boundary correspondence relates quantized bulk invariants defined for the momentum-space with the presence of edge states under OBC in the complementary real-space, since position and momentum are conjugate variables. The conjugate variable of the (reduced) magnetic flux is the (reduced) electric charge, a central relation in the study of quantum electrical circuits [78]. However, and for our purposes, it is not clear what the meaning of OBC in a “charge-space” could be, if any, and what would correspond to an edge state in this quantized charge-space.
- [58] T. Mizoguchi, Y. Kuno, and Y. Hatsugai, Blocking particle dynamics in a diamond chain with spatially increasing flux, *Phys. Rev. A* **109**, 053315 (2024).
- [59] C. H. Lee, S. Imhof, C. Berger, F. Bayer, J. Brehm, L. W. Molenkamp, T. Kiessling, and R. Thomale, Topoelectrical circuits, *Communications Physics* **1**, 39 (2018).
- [60] S. Liu, R. Shao, S. Ma, L. Zhang, O. You, H. Wu, Y. J. Xiang, T. J. Cui, and S. Zhang, Non-hermitian skin effect in a non-hermitian electrical circuit, *Research* **2021**, 10.34133/2021/5608038 (2021).
- [61] D. Zou, T. Chen, W. He, J. Bao, C. H. Lee, H. Sun, and X. Zhang, Observation of hybrid higher-order skin-topological effect in non-hermitian topoelectrical circuits, *Nature Communications* **12**, 7201 (2021).
- [62] M. Ezawa, Non-abelian braiding of majorana-like edge states and topological quantum computations in electric circuits, *Phys. Rev. B* **102**, 075424 (2020).
- [63] A. Szameit and S. Nolte, Discrete optics in femtosecond-laser-written photonic structures, *Journal of Physics B: Atomic, Molecular and Optical Physics* **43**, 163001 (2010).
- [64] D. Viedma, A. M. Marques, R. G. Dias, and V. Ahufinger, Topological n-root su-schrieffer-heeger model in a non-hermitian photonic ring system, *Nanophotonics* **13**, 51 (2024).
- [65] S. Chen, S. Ke, D. Zhao, J. Ye, Y. Wang, W. Liu, K. Huang, B. Wang, and P. Lu, On-chip photonic localization in aharonov-bohm cages composed of microring lattices, *Nano Lett.* (2024).
- [66] C. J. Flower, M. J. Mehrabad, L. Xu, G. Moille, D. G. Suarez-Forero, O. Örsel, G. Bahl, Y. Chembo, K. Srinivasan, S. Mittal, and M. Hafezi, Observation of topological frequency combs, *Science* **384**, 1356 (2024).
- [67] S. Longhi, D. Gatti, and G. D. Valle, Robust light transport in non-Hermitian photonic lattices, *Scientific Reports* **5**, 13376 (2015).
- [68] J. Schulz, J. Noh, W. A. Benalcazar, G. Bahl, and G. von Freymann, Photonic quadrupole topological insulator using orbital-induced synthetic flux, *Nature Communications* **13**, 6597 (2022).
- [69] C. Jiang, Y. Song, X. Li, P. Lu, and S. Ke, Photonic möbius topological insulator from projective symmetry in multi-orbital waveguides, *Opt. Lett.* **48**, 2337 (2023).
- [70] M. Mazanov, D. Román-Cortés, G. Cáceres-Aravena, C. Cid, M. A. Gorlach, and R. A. Vicencio, Photonic molecule approach to multi-orbital topology (2023), arXiv:2310.03160.
- [71] G. Pelegrí, A. M. Marques, V. Ahufinger, J. Mompart, and R. G. Dias, Second-order topological corner states with ultracold atoms carrying orbital angular momentum in optical lattices, *Phys. Rev. B* **100**, 205109 (2019).
- [72] E. Nicolau, A. M. Marques, J. Mompart, R. G. Dias, and V. Ahufinger, Bosonic orbital su-schrieffer-heeger model in a lattice of rings, *Phys. Rev. A* **108**, 023317 (2023).
- [73] E. Nicolau, G. Pelegrí, J. Polo, A. M. Marques, A. J. Daley, J. Mompart, R. G. Dias, and V. Ahufinger, Ultracold

- atoms carrying orbital angular momentum: Engineering topological phases in lattices, *Europhysics Letters* **145**, 35001 (2024).
- [74] C. Jörg, G. Queraltó, M. Kremer, G. Pelegrí, J. Schulz, A. Szameit, G. von Freymann, J. Mompart, and V. Ahufinger, Artificial gauge field switching using orbital angular momentum modes in optical waveguides, *Light: Science & Applications* **9**, 150 (2020).
- [75] Y. Wang, C. Jiang, M. Zhao, D. Zhao, and S. Ke, Compact topological edge modes through hybrid coupling of orbital angular momentum modes, *Phys. Rev. A* **109**, 063516 (2024).
- [76] L. Madail, S. Flannigan, A. M. Marques, A. J. Daley, and R. G. Dias, Enhanced localization and protection of topological edge states due to geometric frustration, *Phys. Rev. B* **100**, 125123 (2019).
- [77] S. J. Yue, Q. Liu, S. A. Yang, and Y. X. Zhao, Stability and noncentered pt symmetry of real topological phases, *Phys. Rev. B* **109**, 195116 (2024).
- [78] Y.-Q. Li and B. Chen, Quantum theory for mesoscopic electric circuits, *Phys. Rev. B* **53**, 4027 (1996).